Journal of Materials Chemistry A

Accepted Manuscript

This article can be cited before page numbers have been issued, to do this please use: C. Lu, Y. Ma, F. Li, H. Zhu, X. Zeng, W. Ding, J. Wu, T. Deng and J. Zou, *J. Mater. Chem. A*, 2019, DOI: 10.1039/C9TA03038G.

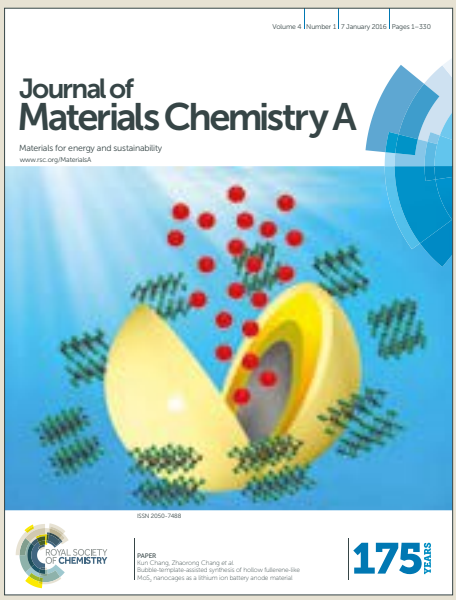

ROYAL SOCIETY OF CHEMISTRY

rsc.li/materials-a

View Article Online
DOI: 10.1039/C9TA03038G

Visualization of fast "hydrogen pump" in core-shell nanostructured Mg@Pt through hydrogen stabilized Mg_3Pt

Chong Lu [a,b†], Yanling Ma[a†], Fan Li[a], Hong Zhu[a,d,e], Xiaoqin Zeng [a, b, c], Wenjiang Ding [a, b, c], Jianbo Wu [a,c,e*], Tao Deng[a,c], Jianxin Zou [a, b, c*]

[a] National Engineering Research Center of Light Alloy Net Forming & State Key Laboratory of Metal Matrix Composites, Shanghai Jiao Tong University, Shanghai, 200240, P. R. China

[b] Shanghai Engineering Research Center of Mg Materials and Applications & School of Materials Science and Engineering, Shanghai Jiao Tong University, Shanghai, 200240, P. R. China

[c] Center of Hydrogen Science, Shanghai Jiao Tong University, Shanghai, 200240, P. R. China

[d] University of Michigan – Shanghai Jiao Tong University Joint Institute, Shanghai Jiao Tong University, 800 Dongchuan Road, Shanghai, 200240, P. R.

[e] Materials Genome Initiative Center, Shanghai Jiao Tong University, 800 Dongchuan Road, Shanghai, 200240, P. R.

†these two author contributes equally to this paper

*Email - zoujx@sjtu.edu.cn

View Article Online
DOI: 10.1039/C9TA03038G

Abstract

A core-shell nanostructured Mg@Pt composite, consisting many of icosahedral Mg particles as the core with nano-sized Pt particles distributed homogeneously on different surfaces, was synthesized through an arc plasma method followed by the generic solid-state method. The microstructures and hydrogen sorption properties of the Mg@Pt composite were carefully investigated in comparison to the pure Mg powder. In particular, dehydrogenation behaviors of the hydrogenated Mg@Pt composite were in-situ observed using the high-resolution transmission electron microscope (HRTEM). The results revealed that Pt on Mg particles showed a "spillover" effect on improving the hydrogen absorption kinetics at the early stage. It then transformed into H-stabilized Mg_3Pt followed by the formation of MgH_2. DFT calculation and in-situ TEM observations demonstrated that H-stabilized Mg_3Pt played a role of "hydrogen pump" effect for the dehydrogenation of MgH_2 and then transformed to Pt after desorption. Through such an effect, the dehydriding kinetics of hydrogenated Mg@Pt composite was improved and the onset dehydrogenation temperature was reduced when compared to those of pure MgH_2 powder.

Keywords: hydrogen storage, core-shell nanostructured Mg@Pt, hydrogen pump, hydrogen stabilized Mg_3Pt

View Article Online
DOI: 10.1039/C9TA03038G

1.Introduction

Hydrogen is widely considered as a promising energy carrier to replace carbon-based fuels due to its environmental-friendly nature, high energy density, and abundant resources[1-4]. With the development of water splitting technique and proton exchange membrane fuel cell (PEMFC), great efforts have been taken to figure out the generation and conversion of hydrogen energy. Except for these two key steps involved in the utilization cycle toward hydrogen energy, hydrogen storage for the purpose of safety and convenience in both usage and transportation is still challenging[3, 5, 6]. Despite that hydrogen-powered electric vehicles have recently emerged as potential choices in global markets, such as Toyota Mirai, Honda Clarity, etc., which used the high pressure tanks (~70MPa) as the hydrogen carrier [7, 8], an optimal hydrogen storage materials with safe, light-weight, and inexpensive characters is still a crucial prerequisite before hydrogen can be globally accepted as a major fuel in the automotive industry[2, 9]. Compared to the high pressure gaseous or low-temperature liquid hydrogen storage, the solid-state hydrogen storage has demonstrated distinct superiority such as high storage capacity, good energy efficiency and safety. These properties render the opportunity of using hydrogen storage materials for onboard or stationary applications[5]. To this end, the solid-state hydrogen storage materials have received great attention in the past decades[10].

Magnesium (Mg) is regarded as one of the most practical candidates among the diverse solid hydrogen storage materials by showing high gravimetric hydrogen capacity of 7.6 wt% as a high earth abundance, non-toxicity and low-cost material[10-14]. Despite these merits of Mg as a solid hydrogen storage material, several challenges hamper its practical applications in hydrogen-powered fuel cell vehicles. Thermodynamically, MgH_2, the stable hydrogen carrier after absorption toward H_2 of Mg, cannot desorb hydrogen unless at high temperatures (above 300 ^oC) due to its high formation enthalpy (~75 kJ/mol H_2) [11]. Besides, hydrogen desorption kinetics is also sluggish in Mg or Mg-based materials since the H diffusion rate in the MgH_2 layer is fairly low[15]. In addition, the strong affinity of Mg with oxygen to form MgO may also hinder the hydrogen sorption process and decrease the hydrogen storage capacity in

Mg[16]. Consequently, extensive researches have been made to overcome these aforementioned challenges through diverse methods, such as nano-confinement, ball milling, alloying, and addition of catalysts in the past decades[16-18]. Recently, nano-structuring become a blooming technique because it can realize the improvements in hydrogen sorption thermodynamics when the particle size is less than ~5nm and kinetics when the particle size is less than ~50nm, respectively[19-21]. These improvements are mainly caused by the increased surface area and shortened hydrogen diffusion length. In addition, a new method involving ball-milling process assisted by dielectric-barrier discharge plasma is devoloped and shows dual-tuning effects on the improvement of both thermodynamics and kinetics for magnesium hydride[22,23]. Besides, adding catalysts is another simple and effective approach to improve the hydrogen sorption properties of Mg[24, 25]. It has been suggested that transition metals (TMs) are good catalysts to enhance the hydrogen sorption properties due to their specific electron configurations of *d*-band[26-29]. Simultaneously, the catalytic performance of supported catalyst could be greatly influenced by its composition, size distribution, and dispersion[30-32]. Consequently, the optimization of decorated catalytic nanoparticles on Mg turns to be critical towards the performance of hydrogen desorption. Recently, building a core-shell structure with Mg core and catalyst decorated on its surface was found to be efficient for enhancing hydrogen storage properties of Mg. For instance, core-shell structured Mg-RE (RE = La, Nd, Gd, Er) composites prepared by an arc plasma method showed improved hydrogen sorption kinetics and reduced oxidation tendency over pure Mg powder [33]. Cui et al. reported that Mg-TM (TM: Ti, Nb, V, Co, Mo, or Ni) composites with core-shell nanostructures exhibited improved hydrogen sorption performances [34].

"Hydrogen pump" effect was considered to play an important role in enhancing the hydrogen desorption properties of MgH_2. The formation of Mg_2NiH_4[34, 35], and the additions of Ce hydrides[36], Pd hydride, and V hydrides[37, 38] can accelerate the hydrogen desorption rate of MgH_2 through such an effect. Lying in the same column as Ni, Pd in periodic table, Pt has also strong affinity to H and is used in fuel cells as hydrogen oxidation catalyst. However, the intermetallic Mg_3Pt phase can be only obtained at a

temperature as high as 1400 ºC[39]. In this study, Mg_3Pt was firstly observed to form at relatively low temperature (300 ºC) in a core-shell structured Mg@Pt via in situ TEM. We also demonstrate a novel "hydrogen pump" effect of Mg_3Pt which can solute H atoms and then transfer them, expediting the desorption rate of MgH_2.

Arc plasma evaporation/condensation of pure Mg followed by generic solid-state method was used to synthesize a core-shell Mg-based composite, Mg@Pt. Compared with the electroless plating approach to synthesize core-shell Mg@TM composites [40-42], the procedure reported in this work is to grow highly dispersed Pt nanoparticles on Mg surfaces through a wet impregnated method. The subsequent gas-solid reduction of Pt precursors was assisted by the forming gas of hydrogen and carbon monoxide which is free of any organic chemicals, thus eliminating the contamination and simplifying the post-washing process of high-yield resultants[43, 44]. The improved hydrogen storage properties, especially reduced H sorption temperatures, of the core-shell structured Mg@Pt composite, were carefully investigated with respect to the pure Mg powder. In particular, the hydrogen desorption process was well observed by in situ TEM technique to study the mechanism and was further investigated by the DFT calculations [45]. Therefore, a better understanding in the intrinsic mechanism of hydrogen desorption is essential to the design of advanced hydrogen storage materials for practical applications.

2. Experimental Methods

2.1 Material synthesis

Pure Mg ultrafine powder without passivation was prepared using an arc plasma evaporation apparatus described in previous works[52-54]. The powder has an average particle size of about 300nm with a typical particle shape of icosahedron[48]. $Pt(acac)_2$ was obtained from Aladdin. Chloroform ($CHCl_3$, AR, ≥ 99.7%) was purchased from Sinopharm Chemical Reagent Co., Ltd.

Firstly, the pure Mg ultrafine powder (0.4145g) was suspended in $CHCl_3$ with vigorous stirring for 30min at room temperature. Secondly, $Pt(acac)_2$ (0.0414g) as the Pt precursor was dissolved in 5ml $CHCl_3$ within 2 min at room temperature and added dropwise to the suspension of Mg followed by stirring for another 30 min. Thirdly, the suspension was dried under vacuum at room temperature, leading to the formation of a

mixture of Mg with sufficiently dispersed $Pt(acac)_2$. Finally, the mixture was reduced by being heated in 30 min to 250 ºC and maintained at the temperature for 30 min in CO/H_2 (150/6 mL/min). To avoid the influence from oxygen and moisture, the first three steps were performed in a glove box with highly purified argon atmosphere. Both the oxygen and moisture contents were maintained at below 1 ppm.

2.2 Materials Characterization

XRD measurement was used to fundamentally understand the phase transformation during hydrogenation and dehydrogenation processes. The morphology and microstructure of the samples were observed by using a FEI Talos F200X transmission electron microscope (TEM), as well as the Energy-Dispersive X-ray Spectroscopy (EDS) attached to TEM. MgH_2 is known to decompose under the electron beam irradiation due to the local irradiation induced temperature rising and vacuum atmosphere [55]. Therefore, high-resolution transmission electron microscope (HRTEM) with the irradiation of beam current of 3 nA has been applied to investigate the decomposition of hydrogenated Mg@Pt composites. A conventional Sievert type Pressure-Composition-Temperature (PCT) volumetric apparatus, manufactured by Shanghai Institute of Microsystem and Information Technology, was used to evaluate the hydrogen storage properties of the composite at various temperatures. For the kinetic measurements, a hydrogen pressure of 2.8 MPa was used at various temperatures for hydrogen absorption and a vacuum condition was set for the desorption. Temperature-Programmed-Desorption (TPD) measurements were performed in the temperature range of 25 ~ 350 ºC starting from a vacuum to verify the hydrogen release properties with a heating rate of 3 ºC/min. The dehydriding behaviors of the hydrogenated composites were also investigated by Synchronous Thermal Analysis [Thermogravimetry/differential scanning calorimetry (TG/DSC), Netzsch STA449F3 Jupiter] under an argon gas flow at a heating rate of 5 ºC/min.

2.3 Density Functional Theory (DFT) Calculations

Density functional theory (DFT) using the projector augmented wave (PAW) method[56] with a kinetic energy cut-off of 520 eV were employed in the Vienna ab-initio simulation package (VASP)[57]. The generalized gradient approximation (GGA) with the

Perdew-Burke-Ernzerhof (PBE) exchange-correlation functional was used in this calculations[58]. Considering that DFT theory is a zero temperature, zero pressure technique, we revised the data based on a given environment at a finite temperature and pressure on the basis of neglecting the effect of temperature and pressure on the solid molecules.

3.Results and discussions

3.1Morphology and microstructure characterizations.

Transmission electron microscopy (TEM), high-resolution TEM (HRTEM) and high-angle annular dark-field scanning TEM (HAADF-STEM) with the energy-dispersive X-ray STEM (EDX-STEM) techniques were employed to further characterize the morphology and microstructure of the as-prepared and hydrogenated Mg@Pt composites. The typical images are shown in Fig. 1. The shapes of Mg particles prepared using the arc plasma method were mainly icosahedron[42,46,47]. The morphology of the observed Mg icosahedral particle exhibits a hexagon shape, which is owing to the well-known structure and the absence of defects and grain boundaries inside this particle[48]. For the as-prepared Mg@Pt composite, the observed Pt nanoparticles having a size of 3 nm (Fig. S1 (a)) were homogeneously dispersed on the Mg polyhedron facets without agglomeration. The well-resolved, continuous fringes can be observed according to the HRTEM image (Fig. 1 (b, c)) and the corresponding Fast Fourier Transform (FFT) can be obtained from the selected areas (I, II) as shown in the insets in Fig. 1 (c). The crystal zone axes for FFT I and II patterns were inferred to be Pt [011] and Mg $[01\bar{1}1]$ according to the standard diffraction patterns for FCC and HCP structures. The angle between Pt [011] and Mg $[01\bar{1}1]$ axes was calculated to be 1.54°, not strictly parallel to each other, resulting in the imperfect FFT patterns. The three different direction patterns represent $(\bar{1}\bar{1}1)$, $(\bar{2}00)$, $(\bar{1}\bar{1}\bar{1})$ planes of Pt in FFT I pattern, while they represent $(\bar{1}101)$, $(0\bar{1}12)$, $(\bar{1}011)$ planes of Mg in FFT II pattern. It can be clearly observed that there exist nearly coherent interfaces between $(1\bar{1}01)$ plane (d = 0.2441 nm) of Mg and (111) plane (d = 0.2296 nm) of Pt from both HRTEM fringes

and FFT patterns. The mismatch between the two planes was calculated to be ~6% according to the equation $\delta = (d_{Mg} - d_{Pt}) / d_{Mg}$ (d is the interplanar spacing), indicating that the existence of this coherent interfaces is rational. In addition, STEM-HAADF image (d) and EDX map of Pt (e) were also employed to prove that the well-dispersed particles were Pt nanoparticles. The selected area electron diffraction (SAED) pattern in Fig. 3 (f) confirms the Mg particle is single crystal for the as prepared Mg@Pt composite. All the above results demonstrated that Pt nanoparticles in-situ formed on the surface of Mg rather than simply mixed with each other. Inevitably, the size of Pt nanoparticles became slightly larger after hydrogenation (Fig. S1 (b)) and dehydrogenation (Fig. S1 (c)) due to the coarsening during the hydrogen sorption cycles performed at high temperatures. However, there was no obviously severe aggregation which demonstrated the thermal stability of Mg@ Pt nanoparticles.

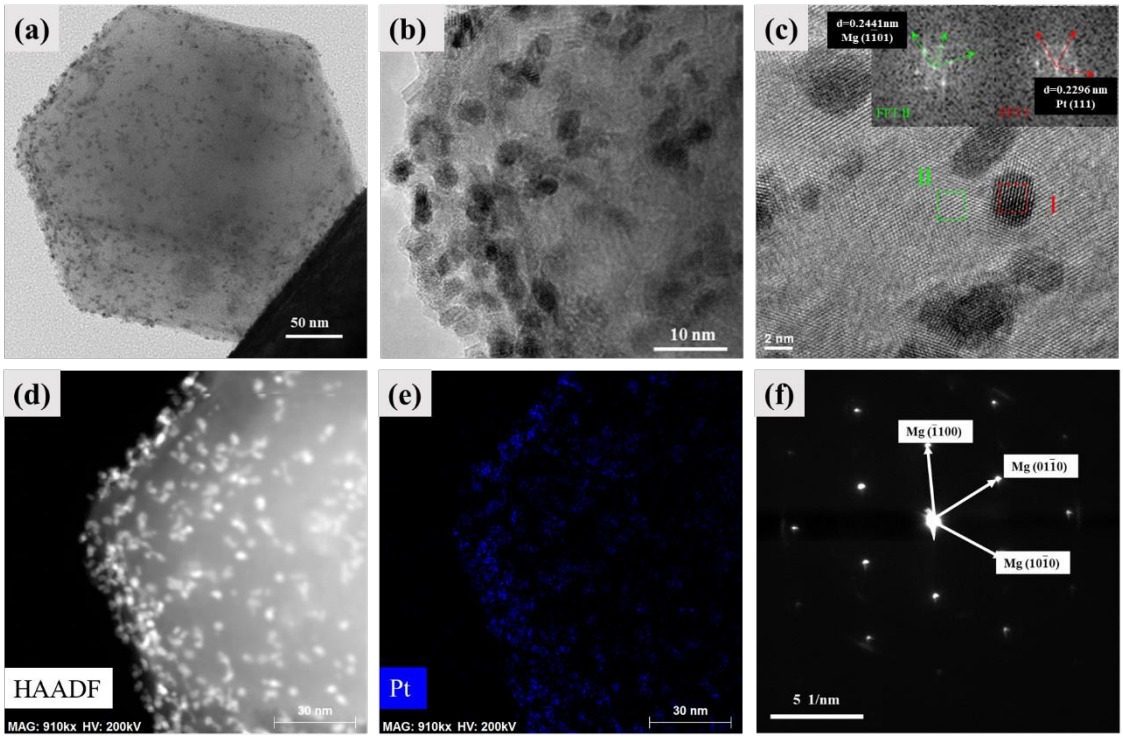

Figure 1. TEM observations of the as-prepared Mg@Pt composite. a, TEM images for theas-prepared Mg@Pt composite. b and c, HRTEM images for the as-prepared Mg@Pt composite. the insets in c display the FFT images of selected area I and II. d, HAADF-STEM image for the as-prepared Mg@Pt composite. e, the corresponding Pt elements map of HADDF-STEM image. f, the corresponding SAED patterns for the as-prepared Mg@Pt composite.

View Article Online
DOI: 10.1039/C9TA03038G

3.2 Hydrogen sorption properties

Target investigating the hydrogen absorption properties, the hydrogen absorption curves for pure Mg and Mg@Pt at various temperatures under 2.8 MPa hydrogen pressure are obtained and displayed in Fig. 2. Before measurements of hydrogen sorption properties, the as-prepared composite was activated through one hydrogen absorption and desorption cycle at 350 ºC. It can be observed that Mg@Pt composite showed faster hydrogen absorption rate than pure Mg (Fig. 2a), especially at relatively lower temperatures (225 and 200 ºC). The Mg@Pt can absorb ~6 wt% of hydrogen to its full capacity in 2h at 225 ºC, while pure Mg powder absorbs ~4.5 wt% of hydrogen under same conditions. The hydrogen storage capacity of Mg@Pt is higher than those obtained in many other Mg-based composites[59-63], as listed in Table S1. The corresponding ln$k$-1000/T plots for pure Mg and Mg@Pt composite were used to estimate the hydrogenation activation energy (E_a). Based on the Arrhenius type linear fittings of ln$k$ vs.1000/T given in Fig. 2(e), the E_a value for Mg@Pt composite is determined to be 82.4 kJ/mol H_2, which is lower than that of pure Mg ultrafine powder (118.2 kJ/mol H_2).

The isothermal hydrogen desorption curves for pure MgH_2 and hydrogenated Mg@Pt at various temperatures (300, 325, 350 and 375 ºC) under vacuum are displayed in Fig. 2 (c) and (d). Clearly, hydrogenated Mg@Pt shows much faster desorption rate than pure MgH_2 at all the testing temperatures. It can be completely dehydrogenated (~6.5 wt% H_2) within 20 min at 350 ºC, while pure MgH_2 requires about 2h at 375 ºC to release the same amount of hydrogen. According to the JMAK model and Arrhenius equation, dehydrogenation activation energy E_d was calculated to be 152.6 and 152.8 kJ/mol H_2 for pure MgH_2 and hydrogenated Mg@Pt composite, respectively (Fig. 2(f)). Though E_d values are quite close, the significant difference in dehydriding rate of the hydrogenated pure Mg and Mg@Pt might be understood concerning the value of pre-exponential factor A. The so-called, frequency factor A, is one of the important dynamic parameters in hydrogen sorption reaction, which depends on the number of active reaction sites (by the dosage of the catalyst, as well as catalyst on the number of active centers)[53, 54]. The hydrogenated Mg@Pt composite shows the much larger value of A

($\ln A$ = 23.2) than that ($\ln A$ = 20.7) of pure MgH_2, thus releasing hydrogen faster due to a large number of active reaction centers. Temperature Programmed Desorption

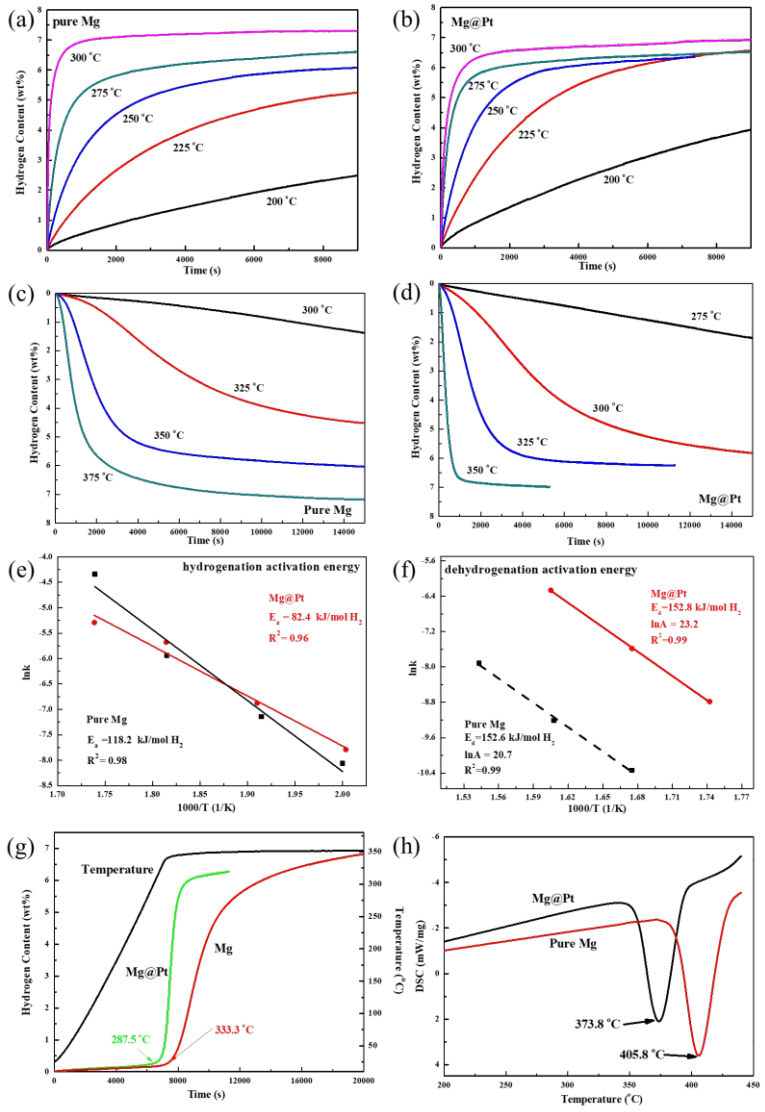

Figure 2. Hydrogen storage properties of the Mg@Pt composite. a, hydrogen absorption curves of pure Mg powder. b, hydrogen absorption curves of Mg@Pt composite. c, hydrogen desorption curves for pure MgH_2 powder. d, hydrogen desorption curves for hydrogenated Mg@Pt composite. e, ln$k$-1000/T fitting plots for hydrogen absorption in pure Mg and Mg@Pt composite. f, ln$k$–1000/T fitting plots for hydrogen desorption in pure MgH_2 and hydrogenated Mg@Pt composite. g, the TPD curves for pure MgH_2 and hydrogenated Mg@Pt composite. h, DSC curves for pure MgH_2 and hydrogenated Mg@Pt composite.

(TPD) and Differential Scanning Calorimetry (DSC) analyses were employed to further explore the hydrogen desorption performance of the hydrogenated Mg@Pt composite as shown in Fig. 2(g, h). The TPD measurement was conducted at a constant heating rate of 3 ºC/min under 0.001 MPa hydrogen pressure, as shown in Fig. 2(g). As can be

seen, the onset dehydrogenation temperatures (T_{des}) of hydrogenated Mg@Pt composite were measured to be 287.5 ºC, lower than that of the pure MgH_2 powder (333.3 ºC). As is shown in Fig. 2 (h), the peak dehydrogenation temperature of hydrogenated Mg@Pt measured from DSC is 373.8 ºC, lower than that of the pure MgH_2 (405.8 ºC). Therefore, it can be concluded that the hydrogen ab/desorption kinetic properties were both improved.

TEM observations were carried out to investigate the microstructure evolution of hydrogenated Mg@Pt during desorption. In the hydrogenated Mg@Pt composite, Mg_3Pt and residual Pt phases can be observed according to the lattice spacings measured from HRTEM fringes (Fig. 3 (b, c)). STEM-EDX maps of Pt (Fig. 3 (e)) also display that the bright dots observed in Fig. 3 (d) are Pt-containing particles. Line scanning (Fig. 3 (d)) was used to analyze the composition of the two chosen particles and the quantitative analysis indicates that the nanoparticles should be Mg_3Pt (Table S2). Therefore, according to the phase change between Pt and Mg_3Pt, it can be deduced that Mg_3Pt may play an important role in improving the hydrogen sorption properties of Mg@Pt composite. As is shown in Fig. 3 (f), the Mg particle turned into polycrystal after hydrogenated. This transformation can be attributed to that each single Pt particle acts as an activation site thus induces the formation of MgH_2 polycrystal. This kind of multi-site catalytic effect from nano Pt particles on Mg single crystal may play an important role in improving the hydrogen sorption properties.

We further use the in situ TEM to investigate the origin of the improvement by real-time imaging the structure and composition evolution of Mg@Pt during the hydrogen desorption process. According to the phase change between Pt and Mg_3Pt observed using TEM technique, Mg_3Pt may play an important role on improving the hydrogen desorption properties of the hydrogenated Mg@Pt composite. To explore the catalytic mechanism of Pt/Mg_3Pt on the hydrogen sorption processes of Mg, in-situ

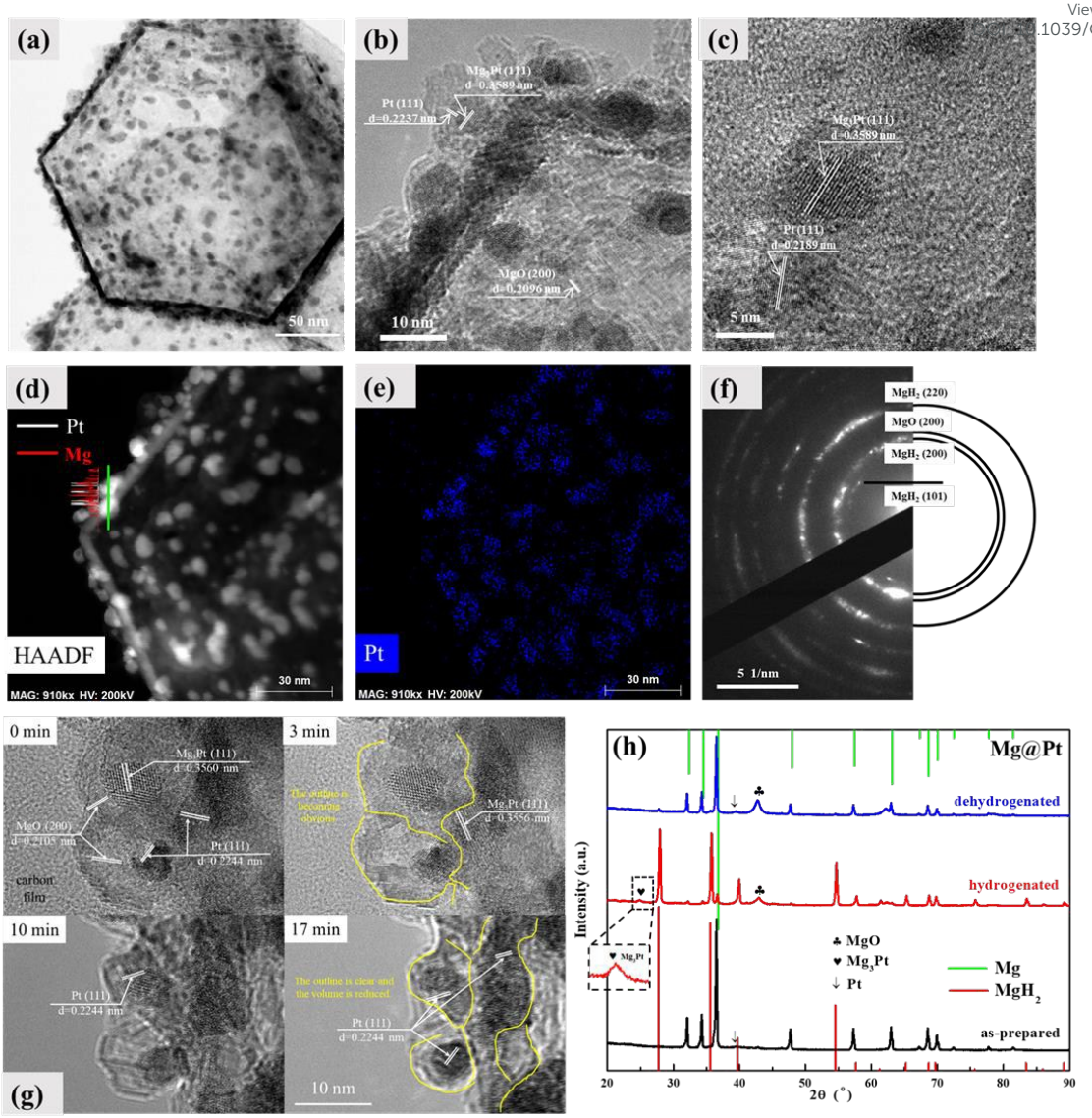

Figure 3. TEM observations of the hydrogenated Mg@Pt composite. a, TEM image for the hydrogenated Mg@Pt composite. b and c, HRTEM images for the hydrogenated Mg@Pt composite. d, HAADF-STEM image for the hydrogenated Mg@Pt composite. The inset in (d) displays the profiles of line-scanning of Mg and Pt. e, the corresponding HADDF-STEM image of the Pt element map. f, the corresponding SAED patterns for the hydrogenated Mg@Pt composite. g, HRTEM images showing the microstructure evolution during the hydrogen desorption process induced by the electron beam radiation in the hydrogenated Mg@Pt composite. h, the XRD profiles of the as-prepared, hydrogenated and dehydrogenated Mg@Pt composite.

high-resolution transmission electron microscopy (HRTEM) was employed to observe the hydrogen desorption process. A series of images with obvious changes (Fig. 3 (g)) were acquired in real-time. Additional images with more details were shown in Fig. S3. Mg_3Pt, Pt and MgO phases can be identified according to the spacings of lattice fringes at 0 min. After irradiation under beam current of 3 nA for 3 min, the inner Pt particle turned into Mg_3Pt, and then part of Mg_3Pt transformed into Pt with the continuous

dehydrogenation at 10 min. The observed area released hydrogen completely after 17 min. A significant volume shrinkage was observed, and all the Mg_3Pt particles turned to be Pt particles. These observations were in good accordance with the XRD results shown in Fig. 3 (h). The hydrogenated Mg@Pt composite was acquired through hydrogenation at 300 ºC under 2.8 MPa hydrogen pressure for 2 h. The dehydrogenated Mg@Pt composite was achieved through dehydrogenation at 325 ºC under vacuum for 2h. A very weak and broad peak from Pt can be detected for the as-prepared Mg@Pt composite, indicating that the Pt particle is extremely fine. X-ray photoelectron spectroscopy (XPS) profiles also showed 4f7/2 and 4f5/2 peaks of Pt with respect to the binding energies of 70.1 eV and 73.2 eV, demonstrating the existence of Pt in the Mg@Pt composite (Fig. S4). It should be noted that a-new weak peak corresponding to the Mg_3Pt phase appeared in the XRD pattern of the hydrogenated Mg@Pt composite. After dehydrogenated, the diffraction peak from Mg_3Pt disappeared and a broader weak peak from Pt was detected again. It has been established that Mg_3Pt is a stoichiometric intermetallic compound[47] and can be obtained from the reaction between Mg and Pt under extreme conditions (1400 ºC, 1.25 GPa) [35]. Therefore, the relatively easy formation of Mg_3Pt after hydrogenation might be attributed to the presence of both nanosized Pt and hydrogen atmosphere. Combining the results of in-situ observations and XRD results, hydrogen might play a major role for the formation of Mg_3Pt. To better understand such a process, DFT calculations were carried out to explore the stability of Mg_3Pt with and without hydrogen.

Considering the small radii of hydrogen atoms, they should occupy the interstitial sites in the Mg_3Pt lattice. Therefore, models with one H atom occupied at a tetrahedral site and an octahedral site were built and shown in Figs. 5 (a) and (b), respectively. Defect formation energy (E_f), which is a key physical parameter to describe the stability of point defects in Mg_3Pt. So we calculated their formation energies as follows:

$$E_f(T, p) = E_{Mg_3Pt\text{-}H} - 3\mu_{Mg} - \mu_{Pt} - \mu_H(T, p) \quad (1)$$

where E_f is the defect formation energy, $E_{Mg_3Pt\text{-}H}$ is the total energy of Mg_3Pt with interstitial H atoms, μ_{Mg} and μ_{Pt} are the chemical potential of Mg and Pt, respectively, and $\mu_H(T, p)$ are the chemical potential of H atom at finite temperature and pressure.

In this case, we can conclude the defect formation energy dependence on hydrogen pressure based on the above calculation (Fig.4 (c)). It shows a tendency towards lower defect formation energy of H atom with increasing hydrogen partial pressure. The calculation results agree well with the results obtained about Mg_3Pt in the experiment.

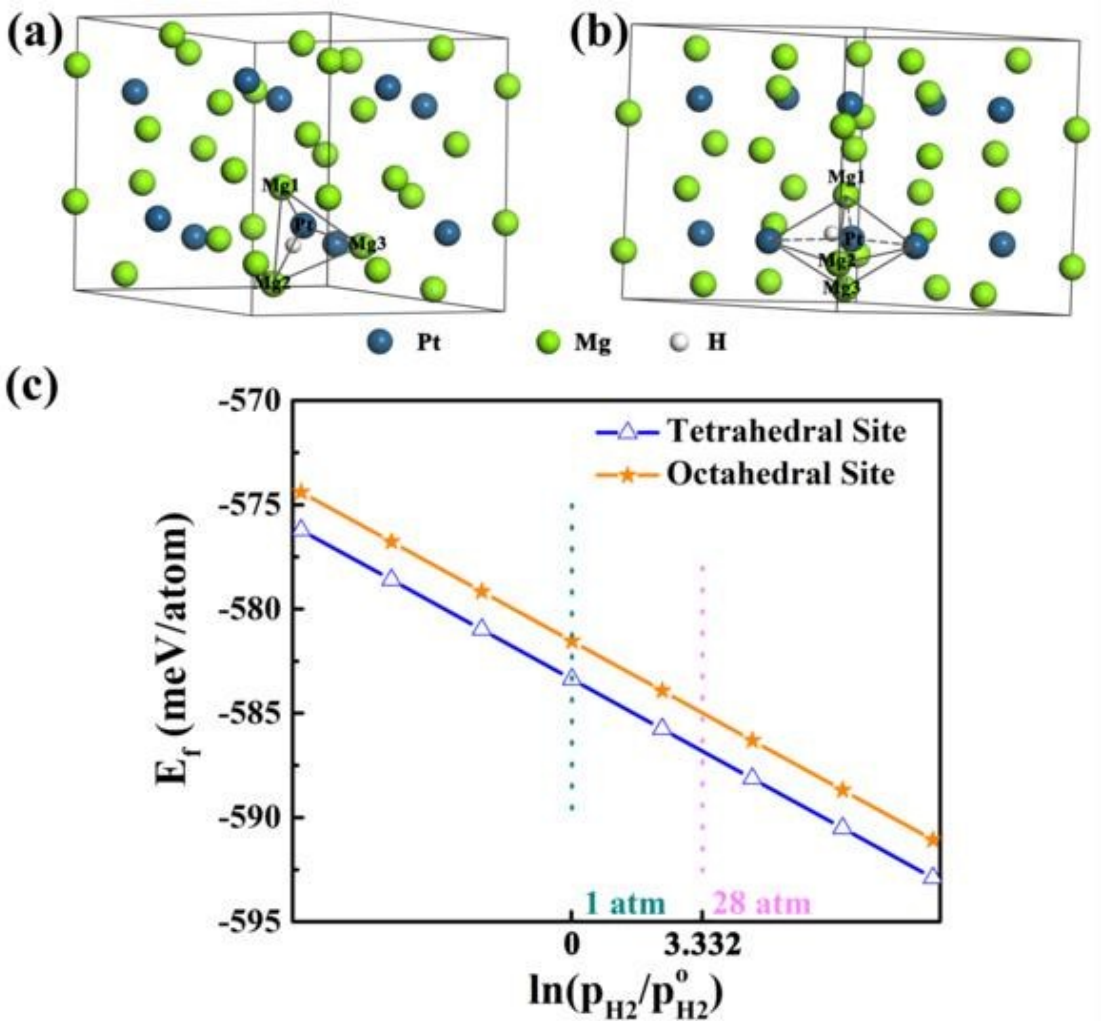

Figure 4. The theoretical calculation results about the Mg@Pt composite. a, interstitial hydrogen atom in the tetrahedral sites of Mg_3Pt. b, interstitial hydrogen atom in the octahedral sites of Mg_3Pt. c, the defect formation energy of H atom dependence on hydrogen pressure at the tetrahedral and octahedral site, respectively.

It can explain that Mg_3Pt can be generated with the increasing hydrogen pressure because of lower defect formation energy of H and that Mg_3Pt will disappear under the vacuum condition due to the relative instability of H defect existence in Mg_3Pt. To elucidate the effect of H atom on bonding of Mg and Pt, we analyzed the change of bond length of Mg or Pt around H atom shown in Table S3 and the corresponding atom

View Article Online
DOI: 10.1039/C9TA03038G

numbers are labeled in Fig. 4 (a, b). The increasing distance of Mg-Mg or between Pt-Mg after H doping demonstrated that the presence of hydrogen will weaken bond strength among metal atoms. Therefore, both theoretical and experimental results account for the appearing and vanishing of Mg_3Pt based on the change of hydrogen partial pressure. The sensitivity to hydrogen indicates that H stabilized Mg_3Pt may act as a "hydrogen pump" to transfer H atoms during the dehydrogenation process, thus accelerating the hydrogen release rate.

The hydrogen sorption process is a gas-solid reaction whose reaction rate is affected significantly by the gas-solid interface. Both the hydrogen absorption and desorption kinetics for Mg@Pt composite were improved in the light of the measured hydrogen sorption properties. A catalytic mechanism during the whole hydrogen absorption and desorption process was proposed according to the observed phase and microstructure changes. As shown in Fig. 5, the typical morphology of Mg ultrafine particle is icosahedron with 20 facets to minimize its surface energy[44]. Using the generic solid reaction method, nano Pt was decorated homogeneously on all the facets of Mg icosahedrons as shown in (a). These nano Pt particles play the catalytic role for hydrogen sorption in Mg according to the XRD analyses and TEM observations. At the initial stage of the hydrogen absorption process (as shown in Fig. 5 (b)), the catalytic mechanism is mainly the "spill over" effect (Fig. 5 (b′)). That is, Pt nanoparticles are the active centers, which decrease the dissociation energy of hydrogen molecular and transfer hydrogen atoms to Mg, induce the formation of nano MgH_2. Along with the continuous hydrogen absorption, a small portion of Pt particles will transfer into Mg_3Pt particles due to the diffusion of adjacent Mg atoms and the existence of H atoms. Consequently, MgH_2 and H stabilized Mg_3Pt formed at the end of the hydrogen absorption process (Fig. 5 (c)). During the initial stage of hydrogen desorption process, H atoms in Mg_3Pt go out from there interstitial tetrahedral and octahedral sites, while H atoms/ions in MgH_2 can pass through the interface between MgH_2 and Mg_3Pt and enter into Mg_3Pt to stabilize it (Fig. 5 (d)). Such a process continuously takes place until MgH_2 is completely dehydrogenated. With the release of H atoms, Mg_3Pt will transform into Pt without H atoms (Fig. 5 (e)). Some Mg atoms diffuse out from Mg_3Pt will cover

on the surface of Pt particles (Fig. 5 (e′)), forming a specific structure of Pt core and Mg shell, as observed in TEM image of Fig. 3 (b). Such a structure may reversibly change to H stabilized (soluted) Mg_3Pt during hydrogen absorption. Therefore, Mg_3Pt plays a role of "hydrogen pump" to transfer H atoms (Fig. 5 (e′)), accelerating the dehydriding rate of the hydrogenated Mg@Pt composite. In addition, the accelerated hydrogen ab/desorption processes can also be attributed to the large number of phase boundaries between Mg_3Pt/Pt and Mg, providing more diffusion paths for H atoms.

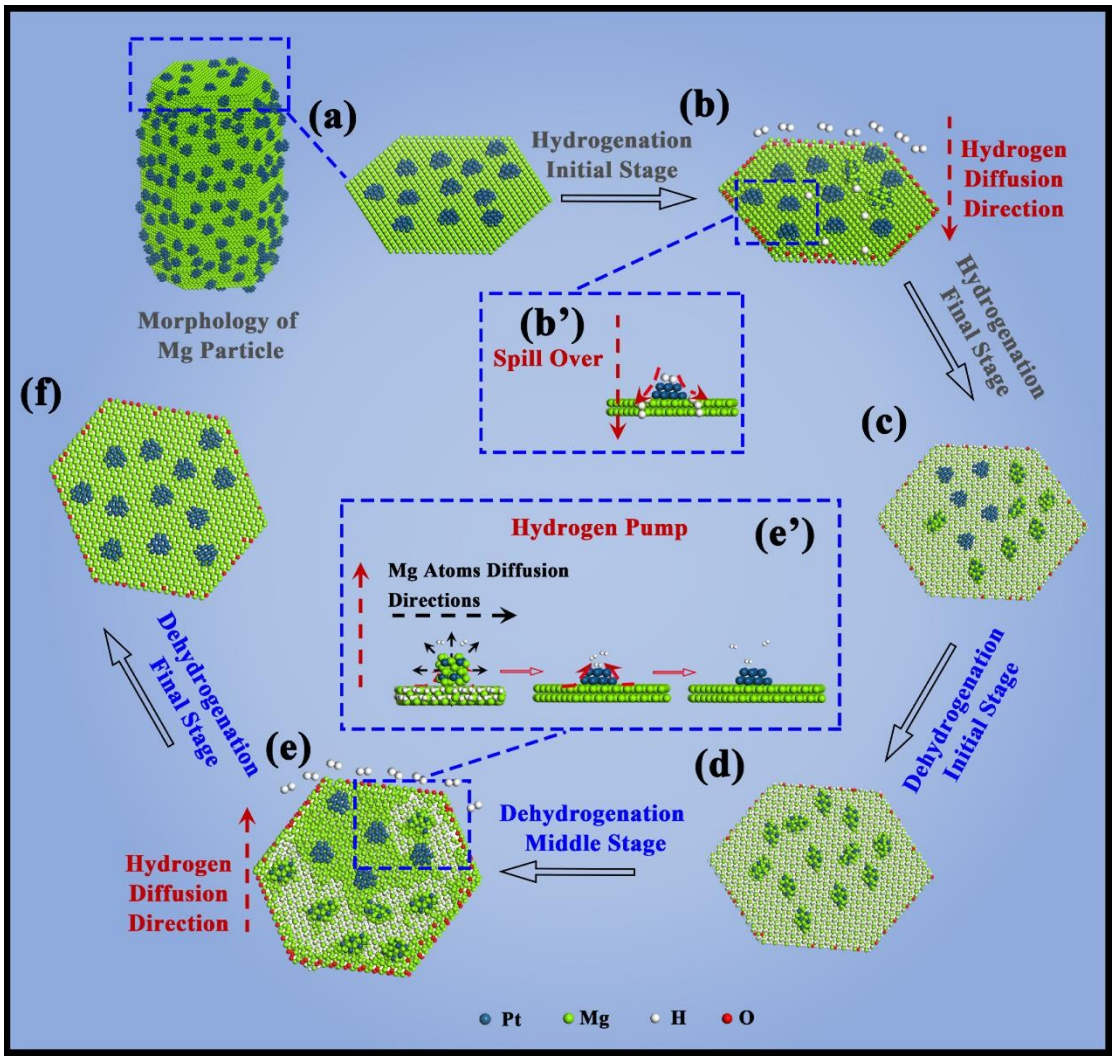

Figure 5. The phase and morphology change and catalytic mechanism during hydrogen ab/desorption processes of the Mg@Pt composite.

4.Conclusions

In the present work, a core-shell nanostructured Mg@Pt composite was synthesized through an arc plasma method followed by the generic solid-state method. The

microstructures and hydrogen sorption properties of the Mg@Pt composite powder were carefully investigated in comparison to the pure Mg powder. Hydrogen absorption kinetics of Mg ultrafine particles can be improved with the decoration of nano Pt particles on them. This can be attributed to the "spill over" effect of Pt, decreasing the hydrogen dissociation energy. Hydrogen desorption behaviors of the hydrogenated Mg@Pt composite are in-situ observed in HRTEM. The results reveal that nano Pt on Mg transformed into H-stabilized Mg_3Pt followed by the formation of MgH_2. DFT calculation and in-situ TEM observations showed that H-stabilized (soluted) Mg_3Pt played a role of "hydrogen pump" effect for the dehydrogenation of MgH_2 and then transformed to Pt after desorption. Through such an effect, the dehydriding kinetics of hydrogenated Mg@Pt was improved and dehydrogenation temperature was lowered down when compared to the pure MgH_2 powder.

Acknowledgment

Prof. Zou would like to thank the support from the National Science Foundation (No. 51771112), the Shanghai Science and Technology Commission under No. 14JC1491600 and Shanghai Education Commission "Shuguang" scholar project (16SG08). J. B. W thanks the thousand talents program for distinguished young scholars from Chinese government, the National Science Foundation of China (21875137, 51521004, and 51420105009), start-up fund (JBW) from Shanghai Jiao Tong University, and the computing resources from Shanghai Jiao Tong University Supercomputer Center.

View Article Online
DOI: 10.1039/C9TA03038G

References

1. L.Schlapbach, Züttel A, *Nature*, 2001,**414**, 353-358.

2. L. Schlapbach, *Nature*, 2009, **460**, 809-811.

3. T. Sadhasivam, H.T. Kim, S. H. Jung, et al., *Sust. Energ. Rev.*, 2017, **72**, 523-534.

4. I. P. Jain, *Int. J. Hydrogen Energy*, 2009, **34**, 7368-7378.

5. H.Reardon, J. M. Hanlon, R. W. Hughes, et al., *Energ. Environ. Sci.*, 2012, **5**, 5951-5979.

6. R. E. Morris, P. S. Wheatley, *Angew. Chem. Int. Ed.*, 2008, **47**, 4966-4981.

7. T. Yoshida, K.Kojima, *The Electrochemical Society Interface*, 2015, **24**, 45-49.

8. M.Matsunaga, T.Fukushima, K.Ojima, *World Electric Vehicle Journal*, 2009, **3**, 820-829.

9. C. Liu, F. Li, L. P. Ma, et al., *Adv. Mater.*, 2010, **22**, 28-62.

10. X.B. Yu, Z. Tang, D.L. Sun, et al., *Prog. Mater Sci.*, 2017, **88**, 1-48.

11. R.Bardhan, A. M. Ruminski, A. Brand, et al., *Energ. Environ. Sci.*, 2011, **4**, 4882-4895.

12. K. F. Aguey-Zinsou, J. R. Ares-Fernández, *Energ. Environ. Sci*, 2010, **3**, 526-543.

13. M. Zhu, H. Wang, L.Z. Ouyang, Int. J. Hydrogen Energy, 2006, 31, 251-257.

14. L.Z. Ouyang, X.S. Yang, M. Zhu, et al., J. Phy. Chem. C., 2014, 118, 7808-7820.

15. M. H. Mintz, Z. Gavra, Z. Hadari, *J. Inorg. Nucl. Chem.*, 1978, **40**, 765-768.

16. K.J. Jeon, H. R. Moon, Anne M. Ruminski, B. Jiang, K. Christian, B. Rizia, J. U. Jeffrey, *Nat. Mater.*, 2011, **10**, 286-290.

17. C. Zlotea, M. Latroche, *Colloid. Surface. A*, 2013, **439**, 117-130.

18. S. D. House, J. J. Vajo, C. Ren, et al., *Acta Mater.*, 2015, **86**, 55-68.

19. T. K. Nielsen, F. Besenbacher, T. R.Jensen, *Nanoscale*, 2011, **3**, 2086-2098.

20. N. S. Norberg, T. S. Arthur, S. J. Fredrick, et al., *J. Am. Chem. Soc.*, 2011, **133**, 10679-81.

21. R. W. P. Wagemans, J. H. v. Lenthe, P. E. d. Jongh, et al., *J. Am. Chem. Soc.*, 2005, **127**, 16675-16680.

22. L.Z. Ouyang, Z. Cao, H. Wang, et al., J. Alloys Compd., 2017, 691, 422-435.

23. D. Wu, L.Z. Ouyang, C. Wu, et al., J. Alloys Compd., 2017, 690, 519-522.

24. J. C. Crivello, R. V. Denys, M. Dornheim, et al., *Appl. Phys. A-Mater*, 2016, **122**, 85.

25. C. J. Webb, *J. Phys. Chem. Solids*, 2015, **84**, 96-106.

26. N. Hanada, T. Ichikawa, H. Fujii, *J. Phys. Chem. B*, 2005, **109**, 7188-7194.

27. G. Liang, J. Huot, S. Boily, et al., *J. Alloys Compd.*, 1999, **292**, 247-252.

28. W. Oelerich, T. Klassen, R.Bormann, *J. Alloys Compd.*, 2001, **322**, L5-L9.

29. A. Roy, A. Janotti, C. G. van de Walle, *Appl. Phys. Lett.*, 2013, **102**, 033902.

30. Y. Zhou, D. E. Doronkin, M. Chen, et al., *ACS Catal.*, 2016, **6**, 7799-7809.

31. E.Alayon, J.Singh, M.Nachtegaal, et al., *J. Catal.*, 2009, **263**, 228-238.

32. P. Wang, X. Kang, H. M.Cheng, *J. Phys. Chem. B*, 2005, **109**, 20131-20136.

33. J.X. Zou, X.Q. Zeng, Y. J. Ying, et al., *Int. J. Hydrogen Energy*, 2013, **38**, 2337-2346.

34. J. Cui, J. Liu, H.Wang, et al., *J. Mater. Chem. A*, 2014, **2**, 9645-9655.

35. W. Su, Y. Zhu, J. Zhang, et al., *J. Alloys Compd.*, 2016, **669**, 8-18.

36. H.J. Lin, J.J. Tang, Q.Yu, et al., *Nano Energy*, 2014, **9**, 80-87.

37. G. Liang, J. Huot, S. Boily, et al., *J. Alloys Compd.*, 1999, **291**, 195-199.

38. W. Oelerich, T. Klassen, R. Bormann, *J. Alloys Compd.*, 2001, **322**, L5-L9.

39. K.J. Range, P. Hafner, *J. Alloys Compd.*, 1992, **183**, 430-437.

40. C. Lu, J.X. Zou, X.Q. Zeng, et al., *Int. J. Hydrogen Energy*, 2017,**42**, 15246-15255.

41. C. Lu, J.X. Zou, X. Shi, et al., *Int. J. Hydrogen Energy*, 2017, **42**, 2239-2247.

42. J.X. Zou, S. Long, X. Chen, et al., *Int. J. Hydrogen Energy*, 2015,**40**, 1820-1828.

43. C. Zhang, S. Y. Hwang, A. Trout, et al., *J. Am. Chem. Soc.*, 2014,**136**, 7805-7808.

44. Y. Ma, W. Gao, H. Shan, et al. , *Adv. Mater.*, 2017, **29**, 1703460.

45. J. Wu, H. Shan, W. Chen, et al., *Adv. Mater.*, 2016, **28**, 9686-9712.

46. J.X. Zou, S. Long, L. Zhang, et al., *Materials Transactions*, 2014, **55**, 1156-1160.

47. S. Long, J.X. Zou, Y. Liu, et al., *J. Alloys Compd.*, 2013, **580**, S167-S170.

48. Q. Yu, L. Qi, R. K. Mishra, et al., *Appl. Phys. Lett.*, 2015, **106**, 261903.

49. K. J. Laidler, *J. Chem. Educ.*, 1984, **61**, 494.

50. P. D. Garn, *J. Therm. Anal.*, 1975, **7**, 475-478.

51. A. A. Nayeb-Hashemi, J. B. Clark, *Bulletin of Alloy Phase Diagrams*, 1985, **6**, 533-

View Article Online
DOI: 10.1039/C9TA03038G

544.

52. H. Shao, Y. Wang, H. Xu, et al., *Mat. Sci. Eng. B-Solid*, 2004, **110**, 221-226.

53. H. Shao, H. Xu, Y. Wang, et al., *Nanotechnology*, 2004, **15**, 269-274.

54. J.X. Zou, H.Q. Sun, X.Q. Zeng, et al., *J. Nanomater.*, 2012, 1-8.

55. N. Kawamoto, D. M.Tang, X. Wei, et al., *Microscopy (Oxf)*, 2013,**62**, 157-175.

56. G. Kresse, D. Joubert, *Phys. Rev. B*, 1999, **59**, 1758-1775.

57. G. Kresse, J. Furthmüller, *Phys. Rev. B*, 1996, **54**, 169.

58. J. P. Perdew, K. Burke, M. Ernzerhof, *Phys. Rev. B*, 1994, **50**, 17953-17979.

59. M. Ma, R. Duan, L.Z. Ouyang, et al., *J. Alloys Compd.*, 2017, **691**, 929-935.

60. L.Z. Ouyang, X.S. Yang, H.W. Dong, et al., *Scripta Mater.*, 2009, **61**, 339-342.

61. H.J. Lin, L.Z. Ouyang, H. Wang, et al., *Int. J. Hydrogen Energy*, 2012, **37**, 14329-14335.

62. D. Wu, L.Z. Ouyang, C. Wu, et al., *J. Alloys Compd.*, 2015, **642**, 180-184.

63. D. Wu, L.Z. Ouyang, C. Wu, et al., *J. Alloys Compd.*, 2017, **690**, 519-522.